

Far field sheaths from waves in the ion cyclotron range of frequencies

J. R. Myra, D. A. D'Ippolito, and M. Bures

Citation: [Physics of Plasmas \(1994-present\)](#) **1**, 2890 (1994); doi: 10.1063/1.870529

View online: <http://dx.doi.org/10.1063/1.870529>

View Table of Contents: <http://scitation.aip.org/content/aip/journal/pop/1/9?ver=pdfcov>

Published by the [AIP Publishing](#)

Articles you may be interested in

[Selfsimilar sheath expansion from a segmented planar electrode](#)

Phys. Plasmas **3**, 2461 (1996); 10.1063/1.871707

[Sheath evolution in a negative ion plasma](#)

Phys. Fluids B **5**, 3813 (1993); 10.1063/1.860599

[Sheath dynamics induced by ionacoustic rarefaction wave](#)

Phys. Fluids B **5**, 3441 (1993); 10.1063/1.860637

[Bifurcations and chaos in a currentcarrying ion sheath](#)

Phys. Fluids B **4**, 3573 (1992); 10.1063/1.860365

[The effects of radio frequency waves on the sputtering of ion cyclotron resonance heating antenna Faraday shields](#)

J. Vac. Sci. Technol. A **5**, 2301 (1987); 10.1116/1.574440



Vacuum Solutions from a Single Source

- Turbopumps
- Backing pumps
- Leak detectors
- Measurement and analysis equipment
- Chambers and components

PFEIFFER  **VACUUM**

Far field sheaths from waves in the ion cyclotron range of frequencies

J. R. Myra and D. A. D'Ippolito

Lodestar Research Corporation, 2400 Central Avenue, Boulder, Colorado 80301

M. Bures

JET Joint Undertaking, Abingdon, Oxfordshire OX14 3EA, United Kingdom

(Received 3 January 1994; accepted 3 June 1994)

Experimental evidence suggests that unabsorbed wave energy in ion cyclotron range of frequency fast wave (FW) experiments can result in deleterious edge interactions. A model describing the formation of far field sheaths due to FW interaction with material surfaces is presented. Near conductors that do not conform to flux surfaces, an incoming FW causes the generation of a slow wave (SW) component. The E_{\parallel} of the SW drives an RF sheath, in a manner similar to what has been previously discussed for antenna (near field) sheaths. To assess the importance of the proposed mechanism, a heuristic scaling model of the resultant sheath voltage V is developed and compared with a numerical code. The model illustrates the important dependencies of V on the single pass absorption, edge density, FW frequency, FW cutoff location, and limiter/wall geometries and yields qualitative agreement with the experimental observations.

I. INTRODUCTION

Experimental evidence on many tokamaks indicates that in regimes of poor single pass absorption, fast wave (FW) interaction with walls and limiters can lead to increased impurity influxes. These influxes can be distinguished from the antenna-sheath interactions that have been studied previously, and occur in the near field region of the launcher.¹⁻⁸ The near field interactions are sensitive to conditions local to a given antenna, such as plasma density and local antenna power. They result in sputtering of the Faraday screen, which can directly contaminate the plasma. Far field interactions depend on global characteristics of the plasma, such as total radio frequency (RF) power and absorptivity of the plasma to the launched waves, factors which determine the intensity of electric fields in the far field zone at the walls and limiters. In addition, far field interactions would be expected to be sensitive to general edge conditions in the scrape off layer, where the waves, material surfaces, and plasma coexist. The relative importance of near field and far field interactions can therefore depend on many factors, and demands a quantification of far field effects similar to what has already been undertaken for the near field processes.^{4,5}

Experimental evidence of far field wave interactions has been seen on several tokamaks. On the Joint European Torus (JET)⁹ before the introduction of a beryllium first wall, poor single pass absorption of the ICRF (ion cyclotron range of frequencies) waves was found to lead to disruption in severe cases.¹⁰ Direct measurements in the edge plasma also showed that both electric and magnetic fields in the edge were larger in regimes of poor single pass absorption.^{10,11} In the Axisymmetric Divertor Experiment (ASDEX)¹² RF induced impurities¹³ were found in the plasma that could not have come from near field sheath¹⁻⁸ processes.

Theoretical work has been motivated by these and related observations.¹⁴⁻¹⁷ In this paper, the interaction of ICRF with a conducting wall or limiter of a tokamak is examined, expanding upon the discussion and calculations presented in Ref. 17. We first consider some of the experimental data

from JET and then move to the development of a theoretical model which focuses on the generation of slow waves (SW) and the subsequent formation of far field RF sheaths.

The present hypothesis may be summarized as follows.

(i) A launched FW from the antenna is not completely absorbed on one pass and therefore encounters either the inner wall or limiter on the high field side (HFS) (perhaps after tunneling through the HFS FW cutoff), or more generally, the FW encounters a wall or limiter surface on the high or low field side (LFS) after multiple reflections from either FW or minority cutoffs. (ii) Because the flux surfaces at the edge do not match the conducting surface exactly, a SW component is generated at the wall with concomitant E_{\parallel} as noted by Perkins.¹⁴ (iii) The E_{\parallel} is screened along the field line by the plasma in a characteristic penetration length resulting in a net RF voltage drop along the field line $V = \int ds E_{\parallel}$. (iv) This RF voltage V is the drive for RF sheaths which act to increase impurity sputtering^{4,5} and generate convective cells⁸ by the same mechanisms that are operative in the near field case.¹⁻⁸ In the present work, we expand on items (i)-(iii). SW generation in the edge plasma has also been discussed by Brambilla,¹⁶ invoking a different mechanism.

Our paper proceeds with a discussion of JET experimental results in Sec. II and the development of the theoretical model in Sec. III. In this section, the relevant model problem is identified and solved, first by heuristic arguments, and then by numerical methods in a restricted domain of parameter space. The numerical results and comparison of the heuristic and numerical models are examined in Sec. IV. Applications of the model to experiment are given in Sec. V. In Sec. VI, and in the Appendix, we discuss some additional physics considerations that lie outside the scope of the present work. Finally, the conclusions of the paper are given in Sec. VII.

II. EXPERIMENTAL EVIDENCE

Experimental evidence for the effects of wave energy on the tokamak walls and limiters was apparent and documented in early ICRF experiments on JET.¹⁰ The evidence,

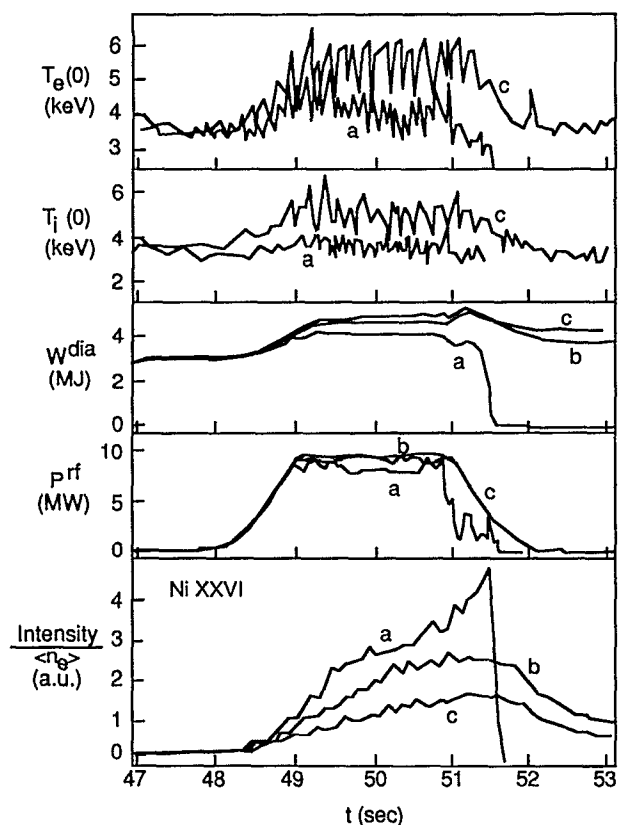


FIG. 1. Evolution of plasma parameters in 3.1 T, 5 MA, D(^3He) discharges with (a) 5 mbars, (b) 15 mbars, and (c) 30 mbars of injected ^3He as a minority species before the RF pulse. The excitation frequency was 33.9 MHz and dipole phasing was used. Shown are the electron and ion temperatures on axis, the stored energy, the ICRF power, and the intensity of a Ni XXVI line normalized to average electron density.

to be presented in Figs. 1 and 2, demonstrates that (i) low single pass absorption can lead to impurity injection, and (ii) low single pass absorption implies increased wave energy at the walls and limiters. We infer that a consistent explanation encompassing both (i) and (ii) could involve impurity injection by wave induced processes at the walls and limiters, which is the subject of our paper. Ideally the evidence for (i) and (ii) would come from the same shot sequence, or at least the same RF heating scenario. Unfortunately, we are forced to make our case from two distinct RF experiments, the nickel influx and disruptions during dipole ^3He minority heating of Fig. 1, and the monopole magnetic probe data of Fig. 2.

We consider Fig. 1 first, which presents the most dramatic demonstration of far field effects, viz., a series of consecutive shots in which the concentration of the minority gas, ^3He , was varied for dipole ICRF heating at similar power levels, and into otherwise similar D target plasmas (3.1 T, 5 MA discharges). The results, taken from Ref. 10, are shown in Fig. 1 for the cases of 5, 15, and 30 mbars of injected ^3He . Experimentally, it is seen that the lower the concentration of minority gas, the lower the electron and ion temperatures, and stored energy, but the larger the concentration of nickel impurities. For the 5 mbars case, the nickel concentration becomes large enough to trigger a disruption at about 51.5 s.

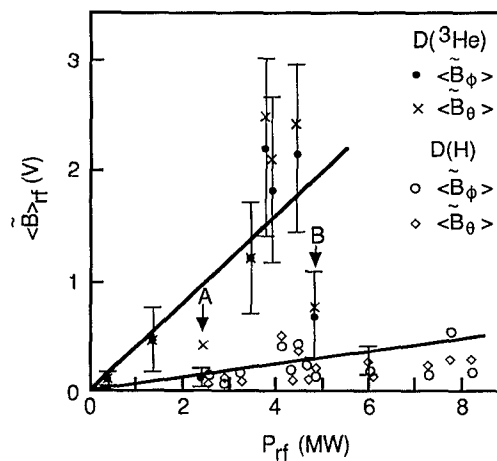


FIG. 2. Amplitude dependence of the magnetic probe signal on the ICRF power in the 3.15 T, 3 MA, D(^3He) and 2.15 T, 2 MA, D(H) discharges with monopole phasing. The time averaged values of toroidal and poloidal components are plotted together with the standard deviations. The point labeled A corresponds to $B_T = 2.8$ T which places the H resonance layer in front of the antenna. The point labeled B corresponds to $B_T = 3.4$ T which introduces the Alfvén resonance layer close to the inner wall.

Carbon influxes (not shown) are also significantly enhanced in the 5 mbars case.

The results are suggestive of an interpretation in terms of far field wave processes. In these experiments, JET was operated with nickel coated antenna screens, and it is believed that a two step process led to nickel injection into the plasma. First, near field sheath-enhanced sputtering^{4,5} of nickel from the antennas resulted in a nickel coating on the walls and limiters. This was evidenced by an observed shot-to-shot increase of more than tenfold in the nickel impurity concentration in the plasma, during the Ohmic phase before the RF pulse, over the course of approximately 70 shots. While there were no spatially resolved nickel influx measurements, it is believed that nickel was spread all around the torus, but more significantly on the low field side, since inner wall limited operation was not commonly used with RF heating. Second, deposited nickel could be released by far field sheath-enhanced sputtering. Thus the nickel concentration in the plasma can be interpreted as resulting from the interaction of unabsorbed waves with the walls and limiters. This interpretation is supported by the signals from the D_α and C_{III} detectors¹⁰ (not shown in Fig. 1) at the walls and limiters which show increases in the 5 mbars case relative to the 30 mbars case. While near field antenna processes may have been occurring together with the far field processes in these experiments, it is difficult to argue that the near field process should have any sensitive dependence on minority concentration. In contrast, the single pass absorption, and hence the far field processes are a sensitive function of minority concentration. For example, in the 5 mbars case, the minority concentration is estimated to be on the order of 0.5%, and the corresponding single pass absorption, as estimated from one-dimensional ray tracing, is only 10%, while in the 30 mbars case the single pass absorption rises to about 30%. Consequently, the minority concentration should significantly af-

fect the unabsorbed wave energy at the plasma edge. The data on heating efficiency in terms of plasma stored energy and temperatures for these shots clearly show that RF absorption is more efficient in the higher concentration case. As further evidence for wave energy being reflected back and forth from the plasma edge, the loading resistance for these shots shows FW eigenmodes even though the antennas were phased as dipoles.

While this data suggests the relevance of far field sheaths to impurity injection, it is likely that other mechanisms are also present. For example, in the 5 mbars case a more energetic minority tail is expected than in the 30 mbars case. Differences in the diffusion of, and sputtering by, this energetic ion component could be responsible for the observed differences in impurity influxes. Additionally, in the 5 mbars case, damping mechanisms competing with core plasma heating, such as parasitic effects at the plasma edge (including, but not limited to RF sheaths), get a larger share of the RF power. The added absorbed energy at the plasma edge may be expected to drive a variety of edge processes that ultimately contribute to the observed impurity influxes. Rather than attempting to rule out any of these other mechanisms, we focus in this paper on motivating and developing a far field sheath model as one important candidate edge physics mechanism that may be operative in low single pass absorption situations.

The motivation for examining far field sheaths comes not only from the preceding minority concentration experiments, but also from direct measurements of the RF edge fields which point to the relevance of single pass absorption. In experiments on JET, probes were employed to detect the edge electric and magnetic fields. In Fig. 5 of Ref. 11, Tagle *et al.* show the results of triple probe measurements of the DC poloidal electric field during minority H and ^3He heating in D majority target plasmas. The edge electric fields are seen to be a factor of 3–10 times larger for the minority ^3He case. This is suggestive of far field wave processes since the single pass absorption is much larger for the D(H) scenario than it is for D(^3He).

Similar results are shown here, in Fig. 2, reproduced from Ref. 10, for the RF magnetic field measured by magnetic probes, for D(H) and D(^3He) heating scenarios. The RF magnetic field is larger for the ^3He minority case, directly demonstrating that low single pass absorption correlates with significant RF wave energy at the edge. The data is given only for monopole phasing because the magnetic probe signals were found to be generally small, and in the H-minority case often unobservable, in dipole phasing unless the probes were dangerously close to the plasma. In these experiments, the magnetic probes were located near the top of the torus (outside the toroidal belt limiters) near $R=2.71$ and $R=3.25$ m, and the magnetic axis was at $R_0=3.25$ m.

While the experimental data available is not sufficient to make a case for specific RF processes at the edge, it is both suggestive and consistent with the far field sheath mechanism that is the topic of the present paper. In the following sections, a model of far field wave interactions with walls and limiters will be developed, and compared qualitatively with the experimental data.

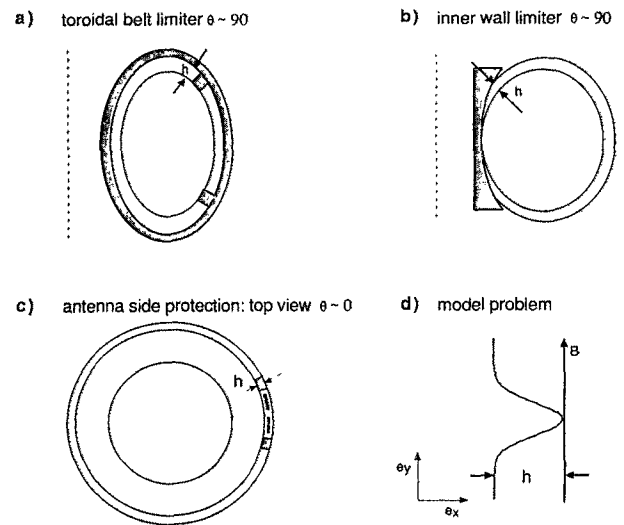


FIG. 3. Geometry of far field sheath interactions: (a) toroidal belt limiters provide the mismatch between the conducting surface and the flux surface, with the toroidal direction being the direction of local symmetry, (b) the inner wall limited case, again with local toroidal symmetry, (c) poloidal limiters, here antenna side protection tiles, are the source of mismatch, with local symmetry in the poloidal direction, (d) a model geometry which encompasses the essential features of (a)–(c), with local symmetry direction out of the plane of the page. In (a)–(d), h is the characteristic mismatch of the conductor and the flux surface.

III. THEORETICAL MODELING

A. Geometry

Far field sheaths occur as a result of the slow wave (SW) that in general must exist when a FW impinges on an irregular conducting boundary, where by irregular we mean that the bounding surface of the conductor and the flux surface are not coincident.¹⁴ Mathematically, this condition may be expressed as

$$\mathbf{e}_n \cdot \mathbf{b} \neq 0, \quad (1)$$

where \mathbf{e}_n is the unit vector normal to the conducting boundary and $\mathbf{b} = \mathbf{B}/B$ is the direction of the equilibrium magnetic field of the tokamak. Several typical situations of interest are shown in Fig. 3. In each case, the wall/limiter geometry has a symmetry direction (at least locally), denoted by the unit vector \mathbf{e}_s , and an angle θ of the magnetic field relative to the conductor, given by

$$\cos \theta = \mathbf{e}_r \times \mathbf{e}_s \cdot \mathbf{b}, \quad (2)$$

where \mathbf{e}_r is a unit vector in the radial direction.

In Figs. 3(a), and 3(b), the limiters are symmetric in the toroidal direction, and the magnetic field angle approaches 90° when \mathbf{B} is purely toroidal, with $\theta \approx 70^\circ - 80^\circ$ being typical of JET operating conditions. Note that the angle θ is normally best thought of as the complement of the angle that the \mathbf{B} field makes with the symmetry direction. It is not the angle of grazing incidence of the \mathbf{B} field on the surface, which approaches zero at the tangency point where the \mathbf{B} field just grazes the surface. For example, for the toroidally symmetric case, the angle is the one between \mathbf{B} and the poloidal direc-

tion which is given by the local pitch of the field lines in the poloidal-toroidal plane (e.g., in the cylindrical tokamak model $\tan \theta = q/\epsilon$).

Figure 3(c) illustrates a case relevant to wave interactions with poloidal limiters, such as might be installed as the main limiters in a tokamak, or as side antenna protection tiles. In this case, the local symmetry direction is poloidal and $\theta \approx 10^\circ - 20^\circ$ is typical. Far field wave interactions with an antenna side protection tile would be of interest when the launched waves reflect back towards the antenna from a fast wave (FW) or minority cutoff in the plasma.

If the magnetic field lines and flux surfaces in Figs. 3(a)–3(c) are transformed to straight lines and planar surfaces, the essential geometry of these systems is that of the schematic model of Fig. 3(d), where the symmetry direction is given by $\mathbf{e}_s = \mathbf{e}_z \equiv \mathbf{e}_x \times \mathbf{e}_y$ and \mathbf{B} lies in the y - z plane. The conducting surface and the flux surface depart by a characteristic distance h , modeled by a Gaussian shaped bump of the leftmost boundary of the domain, in the x direction. The angle θ is 0° when the magnetic field is in the plane of the page, and is 90° when $\mathbf{b} = \mathbf{e}_z$. We imagine that left-going (incoming) FW's are incident on the left conducting boundary from $x = \infty$, and wish to solve for the magnitude of the SW, the induced RF E_{\parallel} , and the net RF voltage drop along the field line $V = \int ds E_{\parallel}$ that is generated by the wave interaction at the wall.

B. Heuristic model

The radial (x) Poynting flux S launched from an antenna is related to the launched FW electric field amplitude at the antenna $E_{\perp a}$ by

$$E_{\perp a} = (16\pi\omega S/k_x c^2)^{1/2}, \quad (3)$$

where \perp is perpendicular to $\mathbf{B} = B(b_y \mathbf{e}_y + b_z \mathbf{e}_z)$, ω is the RF frequency with all waves $\propto \exp(-i\omega t)$, and k_x is the radial component of the wave vector. For the case of inner wall interactions, the single pass transmission coefficient T_{sp} determines how much wave energy gets through to the other side of the torus. For outer wall/limiter interactions that occur as a result of waves reflecting back to the low field side, T_{sp} must be interpreted as the net transmission along the ray as it travels from the antenna, undergoes reflection, and finally arrives at the wall. Introducing a factor R_A , a ratio of areas that accounts for wave focusing and spreading effects in the plane perpendicular to the direction of propagation, and $\alpha \sim \exp(-\int dx |\text{Im } k_x|)$, the tunneling factor through the cutoff (if there is one), the resulting electric field is of order

$$E_{\perp b} = \alpha(R_A T_{sp})^{1/2} E_{\perp a}. \quad (4)$$

At a distance x from a flat conducting wall, the FW electric field therefore takes the form

$$\mathbf{E}_{fw,0} = E_{\perp b} [\exp(-ik_x x) \mathbf{e}_{fw}^- + C \exp(ik_x x) \mathbf{e}_{fw}^+], \quad (5)$$

where C is a constant to be determined from the boundary conditions and \mathbf{e}_{fw}^{\pm} is the FW polarization unit vector for wave number $\pm k_x$ (with k_y and k_z dependencies suppressed). The functional form of $\mathbf{e}_{fw} \equiv \mathbf{e}_{fw}^+$ is given by

$$\mathbf{e}_{fw} = \frac{Q \mathbf{n}_{\perp} + \mathbf{b} \times \mathbf{n}_{\perp}}{[Q \mathbf{n}_{\perp} + \mathbf{b} \times \mathbf{n}_{\perp}]}, \quad (6)$$

with $\mathbf{n}_{\perp} = \mathbf{n} - \mathbf{b} \mathbf{b} \cdot \mathbf{n}$, $\mathbf{n} = \mathbf{k}c/\omega$, $Q = -i\epsilon_x/(n_{\parallel}^2 - \epsilon_{\perp})$, $n_{\parallel} = \mathbf{n} \cdot \mathbf{b} = n_y b_y + n_z b_z$, $\epsilon_{\perp} \equiv 1 - \omega_{pi}^2/(\omega^2 - \Omega_i^2)$, $\epsilon_{\parallel} \equiv 1 - \omega_{pe}^2/\omega^2$, and $\epsilon_x \equiv \omega_{pi}^2 \omega / [\Omega_i(\omega^2 - \Omega_i^2)]$. The first term in Eq. (5) represents the incoming FW; the second term is the reflected wave. The boundary conditions for a conducting wall are that the tangential components of \mathbf{E} vanish. For a flat wall, in the coordinate system of Fig. 3(d), this requires that $E_y = E_z = 0$ at $x = 0$. Since $E_y = 0$ and $E_z = 0$ turn out to be degenerate equations, there results a unique expression for C

$$C = -\frac{\mathbf{e}_z \cdot \mathbf{e}_{fw}^-}{\mathbf{e}_z \cdot \mathbf{e}_{fw}^+} = \frac{n_x - Q(n_z b_y - n_y b_z)}{n_x + Q(n_z b_y - n_y b_z)}. \quad (7)$$

Combining Eqs. (3)–(7) yields a relationship between the launched Poynting flux S and the FW electric field near the wall. For example, for $k_x x \ll 1$, and $n_y = n_z = 0$, or for both negligible in Eq. (7) so that $C \rightarrow 1$, the exponential may be expanded in Eq. (5) to yield

$$\mathbf{E}_{fw,0} = i \mathbf{e}_{fw} (64\pi\omega k_x R_A T_{sp} S)^{1/2} x \alpha / c. \quad (8)$$

In the implementations which follow, the full expressions for $\mathbf{E}_{fw,0}$, with finite $k_x x$, n_y and n_z , are retained. Recall that for the flat wall considered so far, $\mathbf{B} \cdot \mathbf{e}_n = 0$ where \mathbf{e}_n is the unit normal to the wall.

As discussed in the preceding subsection, the flux surfaces at the edge generally do not match the conducting surface due to the presence of limiters or the effect of plasma shaping. A simple model describing this feature is a wall given by the function $x = \xi(y)$, where $\xi \approx 0$ except near a bump of height $\xi \sim h$. Thus h represents the characteristic mismatch of the flux surface and the conducting wall. The significance of the bump is that the tangential components of $\mathbf{E}_{fw,0}$ given by Eq. (5) are no longer zero on the conducting surface $x = \xi$. Consequently, as noted by Perkins,¹⁴ a SW component \mathbf{E}_{sw} must be introduced so that the boundary conditions can be satisfied, viz.,

$$(\mathbf{E}_{fw} + \mathbf{E}_{sw}) \cdot \mathbf{e}_t = 0 = (\mathbf{E}_{fw} + \mathbf{E}_{sw}) \cdot \mathbf{e}_z. \quad (9)$$

Here \mathbf{e}_t and \mathbf{e}_z are two orthogonal unit vectors tangent to the wall, and \mathbf{E}_{sw} is in the direction of the SW unit polarization unit vector

$$\mathbf{e}_{sw} = \frac{P \mathbf{n}_{\perp} + \mathbf{b}}{[P \mathbf{n}_{\perp} + \mathbf{b}]}, \quad (10)$$

where $P \equiv n_{\parallel}/(n_{\parallel}^2 - \epsilon_{\perp})$.

Equation (9) must be satisfied at each point on the boundary. A numerical technique for constructing a solution which accomplishes this will be discussed in the next subsection. The equation is solved by the introduction of additional Fourier components of both the FW and the SW, in the vicinity of the wall. For the heuristic model considered here, it is adequate to apply Eq. (9) to the model geometry at a characteristic point $x \sim x_h$ and consider only a single additional typical Fourier component for each polarization. Denoting the wave initially launched by the antenna (and its reflected counterpart) by subscript 0, as in Eq. (5), and the additional Fourier components by subscript 1, we may esti-

mate the amplitude of the necessary additional FW and SW components from the following system of equations:

$$\mathbf{e}_z \cdot (\mathbf{E}_{fw,1} + \mathbf{E}_{sw,1}) = -\mathbf{e}_z \cdot \mathbf{E}_{fw,0}, \quad (11a)$$

$$\mathbf{e}_t \cdot (\mathbf{E}_{fw,1} + \mathbf{E}_{sw,1}) = -\mathbf{e}_t \cdot \mathbf{E}_{fw,0}. \quad (11b)$$

Note that both \mathbf{e}_t and $\mathbf{E}_{fw,0}$ depend on spatial coordinates, and the polarization vectors for $\mathbf{E}_{fw,1}$ and $\mathbf{E}_{sw,1}$ depend on wave number. For the additional Fourier component's wave number, we employ $k_{z1}=0$, $k_{y1}=\pi/w$, where w is the characteristic width of the bump, and $k_{x1}(k_{y1}, k_{z1})$ is determined from the appropriate FW or SW dispersion relation

$$\text{FW: } n_{\perp}^2(n_{\parallel}^2 - \epsilon_{\perp}) + (n_{\parallel}^2 - \epsilon_{\perp})^2 - \epsilon_x^2 = 0, \quad (12a)$$

$$\text{SW: } n_{\parallel}^2 \epsilon_{\parallel} + \epsilon_{\perp}(n_{\perp}^2 - \epsilon_{\parallel}) = 0. \quad (12b)$$

While the preceding approximations appear to be rather crude, it will be seen that they provide reasonable estimates of the SW field amplitudes under most circumstances, provided that the typical point x_h is chosen with some care. Typically, we chose $x_h = 0.6h$ so that

$$\mathbf{E}_{fw,0} \rightarrow \mathbf{E}_{fw,h} \equiv \mathbf{E}_{fw,0}(x=x_h) \quad (13a)$$

in the right hand side of Eqs. (11) provides a reasonable estimate of the driving fields along the surface of the bump. However, experience has shown that this estimate can fail near isolated points in parameter space where a given component of $\mathbf{E}_{fw,0}(x=x_h)$ vanishes due to a simple zero crossing. In particular, $\mathbf{e}_x \cdot \mathbf{E}_{fw,0}(x=x_h)$ has been found to exhibit such zero crossings at finite k_z . A simple patch for this difficulty, which appears to work well, is to modify the estimate of the x component given by Eq. (13a) to

$$\mathbf{e}_x \cdot \mathbf{E}_{fw,h} \rightarrow C_h \mathbf{e}_x \cdot \mathbf{E}_{fw,0}(x=0),$$

if

$$|\mathbf{e}_x \cdot \mathbf{E}_{fw,0}(x=0)| > |\mathbf{e}_x \cdot \mathbf{E}_{fw,0}(x=x_h)|, \quad (13b)$$

where C_h is an order unity empirical factor taken to be 2.0 in the runs of this paper.

Because the SW introduces a nonzero component $E_{\parallel} \equiv \mathbf{E} \cdot \mathbf{b}$, a voltage drop is induced along the field line $V \sim \int ds E_{\parallel}$. The SW dispersion relation determines the penetration of E_{\parallel} along the field line, from its maximum value somewhere along the surface of the bump, to zero far away from the conducting boundary, in the plasma. To estimate the penetration length in our two-dimensional model, we specify $k_{\perp} \sim \pi/(w+h)$ and solve the SW dispersion relation, Eq. (12b), for the evanescent k_{\parallel} and then define the penetration length as $L_{\text{pen}} \equiv 1/\text{Im}(k_{\parallel})$. Once the size and parallel penetration of E_{\parallel} are known, the induced voltage along the field line is computed as

$$V = 2 \int ds E_{\parallel}(s) = 2E_{\parallel}(x=\xi)L_{\text{pen}}, \quad (14)$$

where the factor of 2 arises because we assume that a given field line intersects two similar limiting surfaces, and we consider the worst case where the phases are such that the RF driving voltages from each surface add.

Equation (14) is the desired equation giving the driving voltage for RF sheaths due to far field wave interaction with

walls and limiters. The magnitude of $E_{\parallel}(x=\xi)$ is estimated from the solution of Eqs. (11) and the parallel projection of the slow wave polarization vector given by Eq. (10). The driving FW fields are given by Eqs. (5) and (13), which in turn are related to the launched Poynting flux by Eqs. (1)–(4). In Sec. V, the heuristic model will be applied to the calculation of typical sheath driving voltages in the JET tokamak. Before proceeding to this application, however, we first digress to verify the validity of the heuristic model by comparing it, as far as possible, with a numerical code, the development of which is now described.

C. Eigenexpansion code

In order to validate the estimates of E_{\parallel} generated by an incident FW of given amplitude, a full eigenexpansion code has been developed. This two-dimensional code solves for the SW generated in the x - y plane, treating z as an ignorable coordinate of the equilibrium. The geometry is that of Fig. 3(d) with periodicity invoked in the y direction (domain length L_y) and x treated on the semi-infinite domain $[0, \infty)$. To begin, consider the general expansion of an arbitrary electric field in terms of plane waves

$$\mathbf{E} = \mathbf{E}^{\text{src}} + \sum_{np} \mathbf{e}_{np} C_{np} X_{np}(x) Y_n(y) Z(z), \quad (15)$$

where an incoming FW source has been explicitly separated off in the first term. In Eq. (15), p is a polarization index corresponding to either FW or SW, and n is a Fourier index for the mode expansion in y . The quantities \mathbf{e}_{np} are the FW and SW polarization vectors given by Eqs. (6) and (10) for $k_y = 2\pi n/L_y$ and $k_x = k_x(k_y, k_z)$ as obtained from the FW or SW dispersion relations of Eqs. (12). Here k_z is a single imposed constant wave vector component since z is ignorable. The separable eigenfunctions for a uniform density plasma in the box are $X_{np}(x) = \exp(ik_{xnp}x)$ with k_{xnp} again calculated from the dispersion relations, $Y_n(y) = \exp(2\pi i n y/L_y)$, and $Z(z) = \exp(ik_z z)$. The dispersion relations give k_x^2 to be purely real. The sign of k_x is chosen to obey the convention that $\text{Re}(k_x) > 0$ when k_x is real, and $\text{Im}(k_x) > 0$ when k_x is imaginary. Thus $X_{np}(x)$ corresponds to waves that are either outgoing or evanescent for $x \rightarrow \infty$ (i.e., into the plasma), in contrast to the source term which takes the form

$$\mathbf{E}^{\text{src}} = \mathbf{e}'_{\nu, \text{fw}} \exp(-ik_{x, \nu, \text{fw}}x) \quad (16)$$

corresponding to either an incoming wave, or one that is evanescent for $x \rightarrow -\infty$. Here the prime on $\mathbf{e}'_{\nu, \text{fw}}$ is a reminder that the polarization is that corresponding to a wave vector with x -component $-k_{x, \nu, \text{fw}} \equiv -k_x(2\pi\nu/L_y, k_z)$, where $n=\nu$ is the launched mode number in the y direction.

In Eq. (15), C_{np} are the unknown mode amplitudes which must be solved for by invoking the boundary conditions

$$\mathbf{E} \cdot \mathbf{e}_t = 0 = \mathbf{E} \cdot \mathbf{e}_z \quad (17)$$

along the boundary $x = \xi(y) = h \sum_m \exp[-(y-a-mL_y)^2/(2w^2)] \approx h \exp[-(y-a)^2/(2w^2)]$, where the sum

over m is introduced to make the wall periodic in the y domain. Without loss of generality, we choose $a = L_y/2$.

The C_{np} can be obtained by defining and minimizing an error function

$$G \equiv \int ds (|E_z|^2 + |E_t|^2), \quad (18)$$

where here ds is a line element along the wall $x = \xi(y)$, $E_z = \mathbf{E} \cdot \mathbf{e}_z$, and $E_t = \mathbf{E} \cdot \mathbf{e}_t$. Minimization of G with respect to the C_{np} leads to the equations

$$\partial G / \partial C_{np}^* = 0, \quad (19)$$

which results in a standard matrix problem for the C_{np} .

This numerical method is easy to implement in a computer code, and is appealing because it circumvents some of the subtle issues associated with irregular boundaries, widely disparate scale lengths, and incoming/outgoing electromagnetic wave boundary conditions that occur in finite difference schemes. However, the rapid evanescence of the higher mode numbers in the x direction limits the accuracy and range of parameter space that can be handled by a restricted basis expansion of the type given by Eq. (15). In particular, when the highest modes retained (typically $n \sim 160$) have imaginary k_x 's and therefore exponentiate many times over the distance h , numerical accuracy is lost and the matrix problem given by Eq. (19) becomes ill conditioned. In the numerical results section that follows, this will manifest itself as a restriction on both h and the proton/electron mass ratio, which sets the spatial scale of the evanescent SW's and FW's. Nonetheless, the code will be adequate for the present purpose of providing (i) verification of the assertion that an incident FW in the geometry of Fig. 3(d) does induce both a SW and an E_{\parallel} , and (ii) a check on the heuristic model of Sec. III B and a guide to applying it to situations of experimental interest.

IV. NUMERICAL SCALING RESULTS

In this section, the results of the heuristic analytical model described in Sec. III B are compared with the results of the numerical code of Sec. III C, and the scaling of the results with four critical parameters is explored. Before proceeding with the scaling studies, the structure of the numerical solution obtained by the two-dimensional code will be examined.

Figures 4(a) and 4(b) show contour plots of $|E_z|$ and $|E_{\parallel}|$ for the base case parameters: $L_y = 10$ cm, $\nu = 0$, $h = 0.5$ cm, $w = 1.0$ cm, $\theta = 60^\circ$, $k_z = 0$ cm $^{-1}$, $f \equiv \omega/2\pi = 33$ MHz, $\omega/\Omega_i = 1.2$, $n_{ea} = 1 \times 10^{12}$ cm $^{-3}$, $m_p/m_e = 32$, and $m_i/m_p = 2$. Here the quoted values of ω/Ω_i and n_{ea} are the values of magnetic field and density at the plasma edge used to calculate the elements of the plasma dielectric tensor. For Fig. 4 the integrations in Eq. (18) were performed with 1800 points, using an 11 point Bode's rule, and the code was run with 121 Fourier harmonics for both the FW and SW. Additional runs with up to 161 Fourier harmonics and even more accurate integrations showed little change in either the contour plots, or the maximum value of $|E_{\parallel}|$ that was generated by the FW. As a check on the accuracy of the solution, the RMS error in

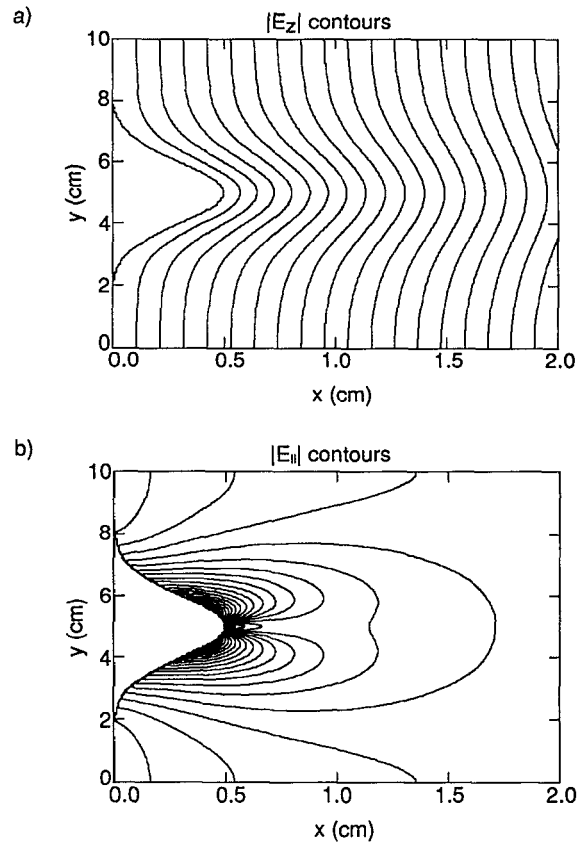


FIG. 4. Numerical solution for fast waves incident from the right on a conducting wall, at left, with a bump of height $h = 0.5$ cm. Shown in (a) are contours of $|E_z|$ which are dominated by the fast wave, and in (b) contours of $|E_{\parallel}|$ due to the slow wave, for the base case parameters given in the main text. Contours are evenly spaced, and in (a) range from a maximum value of 0.047 at the right, to 0 on the wall. In (b), the contours range from a maximum value of 0.0024 near the wall to 0 at the far right.

the boundary conditions was computed from the integrations of Eq. (18). The residual RMS errors on the wall were found to be $\langle E_z^2 \rangle^{1/2} = 5.2 \times 10^{-5}$ and $\langle E_t^2 \rangle^{1/2} = 3.6 \times 10^{-5}$ for the 161 harmonics case. For comparison, the 121 harmonics case gave $\langle E_z^2 \rangle^{1/2} = 3.2 \times 10^{-4}$ and $\langle E_t^2 \rangle^{1/2} = 2.3 \times 10^{-4}$, verifying the convergence of the numerical scheme.

Figure 4(a) may be interpreted in terms of the FW, which dominates the contributions to $|E_z|$. It can be seen that to lowest order the incident FW (from the right) reflects and sets up a standing wave pattern with the conducting wall. The bump in the wall induces perturbations in the FW field patterns, which gradually decay as one moves away from the wall. The higher order harmonics of the FW are evanescent. Note the x and y scales of the figure are quite different. Figure 4(b) present the contours of $|E_{\parallel}|$ which give the SW field pattern. It can be seen that the SW is concentrated at the wall, being evanescent into the plasma for all the harmonics. The maximum value of $|E_{\parallel}|$ occurs near, but not at, the tip of the bump, $y = 5$, $x = h = 0.5$. This feature may be understood by recalling that the wall is locally flat and in the flux surface at the tip of the bump, and that a purely flat wall does not require the generation of the SW to satisfy the boundary conditions. These qualitative features of Figs. 4(a) and 4(b) persist throughout the entire parameter space investigated.

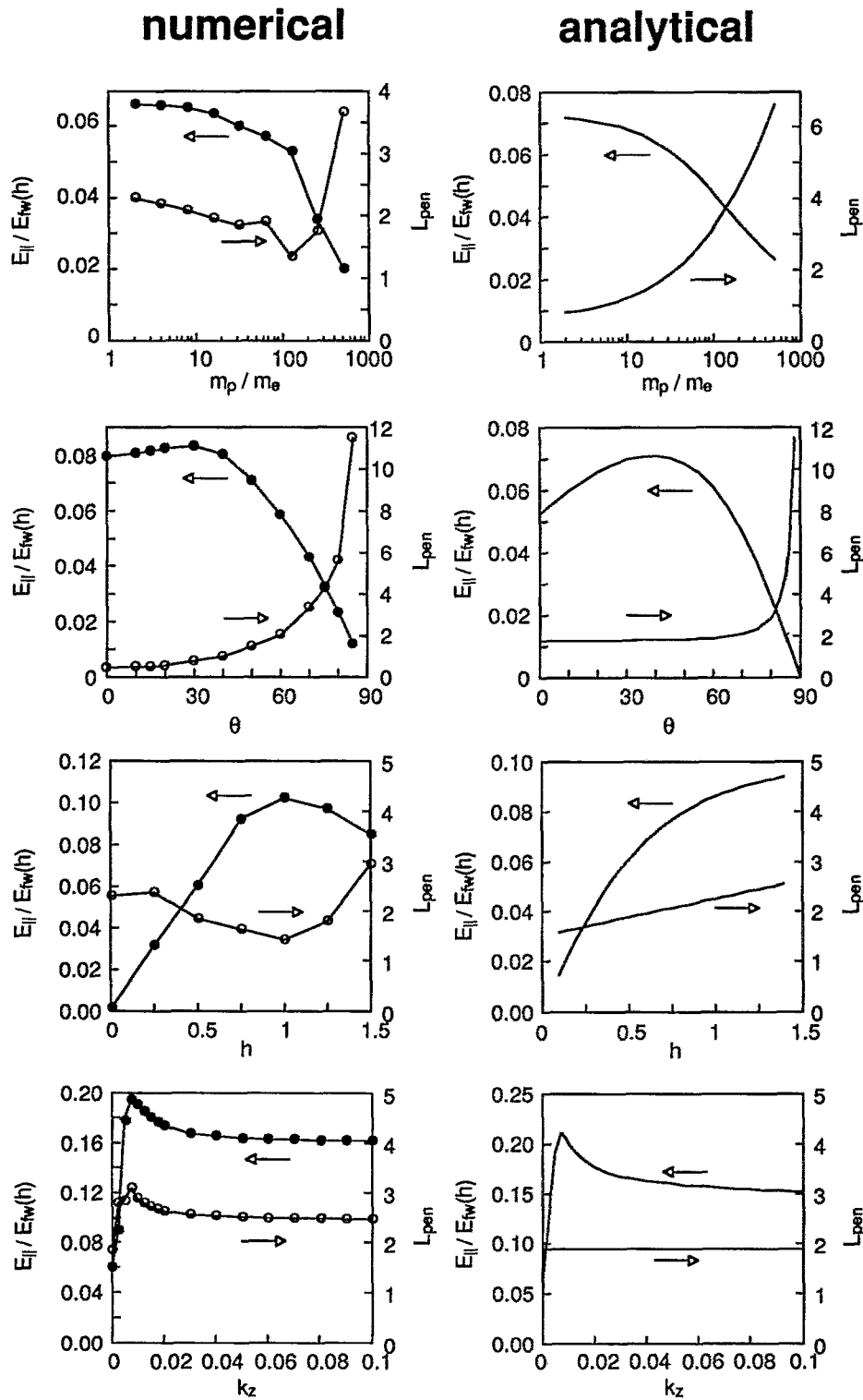


FIG. 5. Numerical and analytical scaling results for the maximum value of the parallel electric field, E_{\parallel} , and its parallel penetration length L_{pen} vs mass ratio, the angle of the magnetic field relative to the surface (in degrees), the mismatch distance h (in cm), and the wave number in the symmetry direction, k_z (in cm^{-1}). Here E_{\parallel} is normalized to $E_{fw}(h)$ as given by Eqs. (13). For the two-dimensional numerical code results on the left, the circles indicate parameters for which the code was run, and the connecting lines between these points are for visualization.

Figure 5 shows the results of scaling studies for the maximum value of the parallel electric field, denoted in the figure label by simply E_{\parallel} , and its parallel penetration length L_{pen} versus mass ratio m_p/m_e , the angle of the magnetic field

relative to the surface θ (in degrees), the mismatch distance h (in cm), and the wave number in the symmetry direction, k_z (in cm^{-1}). Here E_{\parallel} is normalized to $E_{fw}(h) \equiv |E_{fw,h}|$ as given by Eqs. (13) [i.e., with the adjustment of Eq. (13b)]. It

can be seen that the numerical and analytical results show qualitative agreement in the overall scalings and trends, and quantitative agreement to within a factor of 2 or better. The agreement on $E_{\parallel}/E_{fw}(h)$ is actually much better than a factor of 2, which is quite remarkable given the simplistic nature of the heuristic model when compared with the actual two-dimensional code. Here, $E_{\parallel}/E_{fw}(h)$ from the heuristic model has been normalized to the code values with a *single* order unity multiplicative constant ($C_{\text{norm}}=0.63$) which is unchanged for all the scans. The agreement for L_{pen} is somewhat inferior, probably because two-dimensional effects that are difficult to estimate play a role in the shape of the SW field pattern.

Several points on Fig. 5 deserve further comment. First, considering the numerical results for the m_p/m_e scan, it was found that as the mass ratio approaches 1000 the numerical errors become large, with residual RMS values of E_z and E_t on the wall approaching typical values in the plasma. From other runs where the numerical error was large, it was shown that the code tends to underestimate the size of E_{\parallel} (e.g., by comparing the cases of small and large numbers of Fourier harmonics). Thus at the higher mass ratios, the numerical results tend to be artificially lower than the analytical results. Similar remarks hold for h scans, at the higher values of h , where the numerical curve artificially rolls over beyond $h=1$, while the analytical curve continues a gradual rise, until it saturates at much larger values of h (not shown).

A few special points and trends on these curves can be understood from simple considerations. As m_p/m_e increases, the SW polarization is such that the parallel component becomes small compared with the perpendicular component, giving rise to the decreasing trend in $E_{\parallel}/E_{fw}(h)$ versus m_p/m_e in Fig. 5. However, L_{pen} increases with m_p/m_e because of the decrease in k_{\parallel} for a given k_{\perp} , as given by Eq. (12b). Considering the θ dependence, the point at $\theta=90^\circ$ is instructive. For this case, the \mathbf{B} field is coming out of the page, and is everywhere tangent to the wall. Thus SW generation is not necessary to satisfy the boundary conditions $\mathbf{e}_z=\mathbf{e}_t=0$: \mathbf{e}_z is automatically 0 by setting the SW amplitude to zero because $\mathbf{e}_z=\mathbf{b}$ for $\theta=90^\circ$. The divergence in L_{pen} as $\theta\rightarrow 90^\circ$ occurs because $k_{\parallel}\rightarrow 0$ for $k_z=0$. The main feature of note in the h dependence is that as $h\rightarrow 0$, $E_{\parallel}/E_{fw}(h)\rightarrow 0$ as expected for a flat wall. Finally, the k_z scaling shows some structure near $k_z=0.01\text{ cm}^{-1}$, related to the transition from propagation to evanescence for the FW Fourier modes. For these parameters, the launched mode becomes evanescent near $k_z=0.03\text{ cm}^{-1}$; higher modes become evanescent for smaller k_z .

V. APPLICATION TO EXPERIMENT

Having investigated a few of the more important parametric dependencies of E_{\parallel} and L_{pen} , we now turn to applying the model to the calculation of the far field sheath driving voltages for a situation of experimental interest. Because typically the desired values of the mass ratio and bump height, $m_p/m_e=1836$, and $h\geq 5\text{ cm}$, are too large for reliable results from the numerical code, the heuristic model will be employed. Our goal is to assess the importance of the far field sheath mechanism in typical experimental situations,

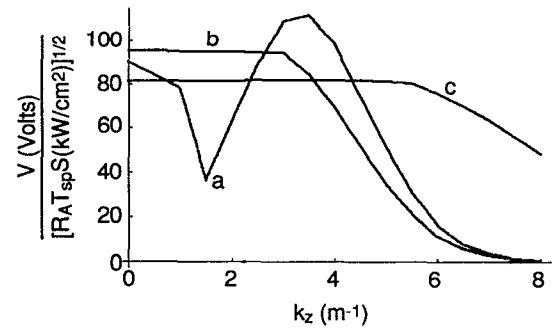


FIG. 6. Heuristic model estimate of the sheath driving voltage V normalized to $(R_A T_{\text{sp}} S)^{1/2}$ for parameters that are illustrative of JET. The two curves (a) and (b) are the result of slightly different forms of the heuristic model, as explained in the main text. Curve (c) employs slightly different parameters which are still illustrative of JET, especially for low field side interactions. These parameters act to reduce the wave evanescence and hence increase the sheath driving voltage at the higher values of k_{\parallel} .

and to get some idea of the physics that influences the size of the resulting sheath voltages. The heuristic model should not be expected to yield results which are numerically accurate; factor of 2 accuracy is expected to be more typical.

A satisfactory quantitative comparison of far field sheath theory with experiment is in any case outside the scope of this paper. To accomplish that, it would be necessary to couple the present RF-wall interaction physics to a single pass absorption model which would also include the physics of reflections from both FW and minority cutoffs. These reflections are important because the reflected waves give rise to far field interactions at the outer wall which may in some cases be more important than the “shine through” interactions of the waves with the inner wall. This is likely the case for the higher k_{\parallel} waves which tend to be cut off farther from the inner wall than the outer wall because of both the $1/R$ dependence of the toroidal field and the $1/R$ upshift in k_{\parallel} that occurs in toroidal geometry (see Fig. 6). Finally, the field distribution near the walls cannot be accurately determined without a two-dimensional code to quantify the effects of wave focusing.

Before embarking on such an ambitious project, it seems prudent to examine the order of magnitude of the far field sheaths from the present model which is essentially local to a given wall. In the following, we show that for reasonable parameters the expected far field sheaths are significant, conceivably large enough to play a dominant role in low single pass absorption experiments such as the ones discussed in Sec. II.

Figure 6 shows the results for the sheath driving voltage V from Eq. (14) versus k_z for parameters which are taken to be illustrative of conditions in JET for far field interactions, viz., $\theta=60^\circ$, $k_y=0$, $w=2\text{ cm}$, $h=5\text{ cm}$, $f=33\text{ MHz}$, $n_{ea}=10^{12}\text{ cm}^{-3}$, $m_i/m_p=2$, $m_p/m_e=1836$, $\omega/\Omega_i=1.2$, $L_n=10\text{ cm}$. Here L_n is a characteristic density gradient scale length inside the last closed flux surface (estimated, not measured) which should be regarded as an average over approximately one FW radial wave length at the edge. The parameter L_n has been employed to calculate the location of the

FW cutoff for the waves near the wall, and hence determines the tunneling factor α in Eq. (4). The voltage shown in the figure has had the simple analytical scaling factor $(R_A T_{sp} S)^{1/2}$ explicitly removed, where R_A and T_{sp} are dimensionless and S has been normalized to 1 kW/cm^2 . The curve labeled (a) in Fig. 6 is the same model used in Fig. 5, which employs the adjustment given by Eq. (13b). For comparison, to give an idea of the sensitivity of the model, a curve labeled (b) is also shown. This curve employs the simple unadjusted result of Eq. (13a).

The curve labeled (c) is for the same model and has the same parameters as for (b) except for $n_{ea} = 2 \times 10^{12} \text{ cm}^{-3}$, $\omega/\Omega_i = 1.7$, $L_n = 5 \text{ cm}$, all of which act to reduce the wave evanescence and hence increase the sheath driving voltage at the higher values of k_{\parallel} . The higher value of ω/Ω_i typifies interactions on the low field side of the torus, while the other parameters are still within the experimentally relevant range. In changing parameters to get from curve (b) to curve (c) the changes in the voltage may be understood as follows. Changing ω/Ω_i from 1.2 to 1.7 causes V_8 , the normalized voltage in Fig. 6 at $k_z = 8 \text{ m}^{-1}$, to rise from essentially zero to nearly 5. With $\omega/\Omega_i = 1.7$, changing L_n from 10 to 5 cm causes an additional rise in V_8 to about 20. The final result of $V_8 \approx 50$ shown in the figure is due to increasing the density from 1×10^{12} to $2 \times 10^{12} \text{ cm}^{-3}$.

For the JET antennas, the typical launched k_{\parallel} is $0\text{--}3 \text{ m}^{-1}$ for monopole phasing and $6\text{--}8 \text{ m}^{-1}$ for dipole phasing. Because of the k_{\parallel} upshift that occurs in toroidal geometry as the waves propagate to the high field side of the torus ($k_{\parallel} R \approx n = \text{const}$), the dipole spectrum is transformed to values approaching 15 to 20 m^{-1} near the inner wall. Strong wave evanescence therefore makes it unlikely that significant inner wall far field sheaths occur in cases (a) or (b) for dipole phasing. However, as curve (c) shows, far field sheaths are not always negligible in dipole phasing, particularly on the low field side. Indeed, one must assume similar parameters to (c) in arguing a far field sheath explanation of the dipole data of Fig. 1.

Employing $R_A T_{sp} S \sim 0.3 \text{ kW/cm}^2$ for high power operation and poor single pass absorption, it can be seen that typical far field sheath driving voltages can easily be several tens of volts in monopole phasing. Similar estimates hold for low field side interactions at high edge densities in dipole phasing. For low edge densities, and especially for high field side interactions, the dipole spectrum is shielded from the wall by the FW cutoff, so the induced voltage is small.

The far field sheath driving voltage, when rectified by the RF sheath processes,¹⁻³ adds to the usual $(3T_e)$ Bohm sheath, and can significantly change the sputtering rate of wall materials into the plasma. The sputtering may be substantially enhanced when the sputtering projectiles are high Z ions, because the impact energy scales like $Z(e\Phi + 3T_e)$. The sensitive dependence of sputtering on impact energy for some different projectiles incident on a carbon limiter is illustrated in Fig. 7. The curves have been calculated from Eq. (6.16) and Table 6.1 of Ref. 18. Figures 6 and 7 together suggest that far field processes could impact the net sputtering rate by changing the operating point of the edge sheaths from below to above the sputtering thresholds.

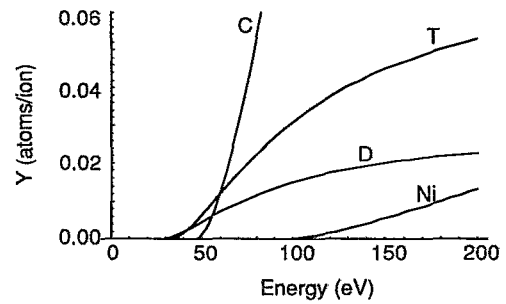


FIG. 7. Sputtering yields for projectile ions impacting on graphite. Shown are results for carbon, tritium, deuterium, and nickel as calculated from Ref. 18.

In addition to increasing the wall sputtering, the sheaths can be responsible for other edge interactions. First, they will drive convective cells in a manner similar to that already proposed for antenna driven (near field) sheaths,⁸ though of smaller amplitude and perhaps over a larger area. Second, they will cause enhancement of the plasma-wall potential drop thereby increasing the ion power flux (and decreasing the electron power flux) into the walls for the same edge density and ion temperature. When the wave driven sheath potential Φ is comparable to $3T_e$, these effects are order unity perturbations on the ohmic plasma equilibrium at the edge.

Qualitatively, the model results correspond to the JET experiments (see Figs. 1 and 2) in two important ways: (i) monopole operation produces more edge interaction than dipole, (ii) edge interaction is stronger in cases of poor single pass absorption ($T_{sp} \sim 1$) than in cases of good absorption ($T_{sp} \ll 1$).

VI. DISCUSSION

In the preceding sections, it has been shown that linear wave physics, in the presence of plasma and a general conducting boundary, results in an induced RF voltage drop along the equilibrium magnetic field lines in the vicinity of the bounding surface. This voltage V is of interest, based on previous studies of near field sheaths,² because it is expected to drive RF sheaths which cause rectification and the generation of a DC sheath voltage of a comparable magnitude. However, the present situation is more complicated than the near field case, because the RF sheaths produced in the far field case modify the boundary conditions seen by the waves. A model of wave interaction with edge sheaths has been proposed by Berro *et al.*¹⁵ In the far field case of interest here, it may be necessary to further treat SW generation and sheath formation self-consistently.

To illustrate more concretely some of the issues at stake, a simple model of sheath boundary conditions for an electromagnetic wave, for the case of a *flat* backwall is given in the Appendix. It is shown that the effect of the sheath is to change the effective boundary conditions seen by the wave from the usual ones given by Eq. (17) to a more complicated set. When the sheaths are dominant, as defined by Eq. (A16), the effective sheath boundary conditions reduce to

$$\mathbf{E} \cdot \mathbf{b} = 0, \quad (20a)$$

$$\mathbf{B} \cdot \mathbf{e}_n = 0, \quad (20b)$$

where we recall that \mathbf{e}_n is normal to the conducting surface. Because Eq. (20a) sets E_{\parallel} to zero at the wall, it may be inferred that no SW is generated in this case. The generalization of Eqs. (20) to the case of a bumpy wall has not yet been achieved, but we expect the self-consistent sheath voltage to lie in between the one discussed in this paper and the limiting case of Eq. (20). The subject of self-consistent inclusion of sheaths in the SW generation problem, and possible mitigation by the sheaths remains an area for future investigation.

Self-consistency of plasma-wall interactions may also be of importance in describing the far field sheaths. Absorption and desorption processes determine the plasma density near the surface. Thus wall conditioning could be important because if n_e at the surface were very low, RF sheaths would be mitigated by space charge depletion, as discussed, for example, in Ref. 2.

So far we have not discussed one simple mechanism by which the driving fields near the walls could be enhanced, viz., by eigenmode formation in the multiple pass regime. This effect works to increase V for a given launched Poynting flux S , approximately by the factor $1/(1-R_{\eta}T_{sp})^{1/2} \approx (Q/\omega\tau)^{1/2}$, where R_{η} is the power reflection coefficient of waves from the walls including finite resistivity effects, or from the wave cutoffs, Q is the cavity quality factor, and τ is a characteristic time for a FW ray to propagate across that portion of the minor radius of the tokamak between reflection points.

VII. CONCLUSIONS

While the present model is a simplified description of far field wave interactions in a tokamak, it seems clear that far field sheath processes can play an important role in low single pass absorption experiments. Through the use of both heuristic arguments and a numerical code, it has been shown that a SW with concomitant E_{\parallel} is generated near the wall, where FWs are incident on a conducting surface that does not match the flux surface. The characteristic features and scalings of E_{\parallel} , its penetration into the plasma, and the resulting induced voltage V have been studied. In low single pass absorption experiments, particularly monopole experiments, but also dipole experiments with sufficiently dense edge plasmas and for low field side interactions, the typical driving voltage V is seen to be comparable to both the usual $3T_e$ Bohm sheath voltage as well as to sputtering thresholds. It is expected that far field sheath processes will contribute to impurity sputtering and modifications of edge potentials, transport, and $\mathbf{E} \times \mathbf{B}$ convection in these cases.

ACKNOWLEDGMENTS

The authors are indebted to J. Jacquinot for many stimulating conversations on ICRF interaction with the plasma edge, and ICRF operation generally on JET. Discussions with F. W. Perkins on the topic of slow wave generation near

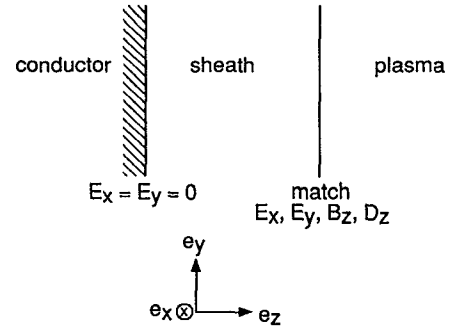


FIG. 8. Model geometry for the calculation of sheath boundary conditions.

conducting boundaries are also gratefully appreciated. The authors also wish to thank the referee for several valuable comments.

This research was supported by U.S. Department of Energy Grant No. DE-FG02-88ER53263.

APPENDIX: SHEATH BOUNDARY CONDITIONS FOR AN ELECTROMAGNETIC WAVE

The fundamental boundary conditions which apply to an electromagnetic wave at a conducting surface are those given by Eq. (17). When a sheath is present at a conducting wall, the wave must penetrate the sheath before contacting the wall. Since the sheath is normally thin compared to other characteristic dimensions of the problem, it is natural to attempt to formulate an alternate set of boundary conditions which can be imposed at the surface of the sheath, and which are equivalent to imposing Eqs. (17) at the wall itself. A derivation of these sheath boundary conditions is presented in the following, for the case of a wave incident on a flat wall.

The geometry is shown in Fig. 8. The conductor is at the left; adjacent to it is a sheath of width Δ ; and then there is a semi-infinite plasma. The coordinate system employed here differs from that of the main text, viz., \mathbf{e}_x and \mathbf{e}_y are tangent to the surface of the conductor, and \mathbf{e}_z is normal to the surface. The main difference between the plasma and the sheath is that the sheath excludes electrons, therefore while ϵ_{\parallel} is large in the plasma due to the parallel electron conductivity, it is of order unity in the sheath. Consequently, a useful qualitative model of the dielectric properties of the sheath is obtained by modeling the sheath as a vacuum layer of the same width.

In the vacuum region, for a plane wave of the form $\exp(i\mathbf{k} \cdot \mathbf{x})$ the dispersion relation is $n^2=1$, and two linearly independent waves (in dimensionless units) are

$$\mathbf{E}_{TE}^{\text{plane}} = \mathbf{e}_z \times \mathbf{n} = (-n_y, n_x, 0), \quad (A1)$$

$$\mathbf{E}_{TM}^{\text{plane}} = \mathbf{n} \times (\mathbf{e}_z \times \mathbf{n}) = (-n_z n_x, -n_z n_y, n_x^2 + n_y^2). \quad (A2)$$

Alternatively, choosing a wave of the form $\exp(ik_x x + ik_y y) \sin(k_z z)$, it is possible to construct solutions which have vanishing tangential components E_x and E_y at $z=0$

$$\mathbf{E}_{TE} = [-n_y \sin(k_z z), n_x \sin(k_z z), 0], \quad (A3)$$

$$\mathbf{E}_{\text{TM}} = [-in_z n_x \sin(k_z z), -in_z n_y \sin(k_z z), (n_x^2 + n_y^2) \cos(k_z z)]. \quad (\text{A4})$$

The general solution for electromagnetic waves in the vacuum region (v), satisfying $E_x^v = E_y^v = 0$ at $z=0$ is therefore

$$\mathbf{E}^v = C_e \mathbf{E}_{\text{TE}} + C_m \mathbf{E}_{\text{TM}}, \quad (\text{A5})$$

with two free constants C_e and C_m . In the electrostatic limit $c \rightarrow \infty$, of interest here because the sheath dimensions are small compared to the free space wavelength, \mathbf{E}_{TE} is not required ($C_e \rightarrow 0$), and $\mathbf{E}_{\text{TM}} \rightarrow -\nabla \Phi$ for some scalar Φ , as evident from Eq. (A4) or Eq. (A2).

Matching $E_x, E_y, D_z \equiv \mathbf{e}_z \cdot \boldsymbol{\epsilon} \cdot \mathbf{E} = \epsilon_{\parallel} E_{\parallel} \cos \theta$ (where $\cos \theta = \mathbf{b} \cdot \mathbf{e}_z$ and $\boldsymbol{\epsilon}$ is the dielectric tensor in the plasma region) and $B_z \equiv \mathbf{e}_z \cdot \mathbf{n} \times \mathbf{E}$ across the plasma–vacuum interface results in the four equations

$$-iC_m n_x n_z \sin(k_z \Delta) = E_x, \quad (\text{A6})$$

$$-iC_m n_y n_z \sin(k_z \Delta) = E_y, \quad (\text{A7})$$

$$0 = B_z, \quad (\text{A8})$$

$$C_m (n_x^2 + n_y^2) \cos(k_z \Delta) = D_z, \quad (\text{A9})$$

where E_x, E_y, B_z , and D_z denote the fields on the plasma side of the interface. We seek from Eqs. (A6)–(A9) two constraints which serve as the effective boundary conditions for the electromagnetic fields on the plasma side. Fortunately, Eqs. (A6)–(A9) are not all independent since Eq. (A8) implies that $n_x E_y = n_y E_x$ making one of Eqs. (A6) and (A7) redundant. Eliminating C_m from the remaining equations results in the desired two constraints (boundary conditions)

$$n_x E_x + n_y E_y \pm i n_z D_z \tan(k_z \Delta) = 0, \quad (\text{A10})$$

$$B_z = 0, \quad (\text{A11})$$

where in Eq. (A10) the $+$ sign applies when \mathbf{e}_z is pointing into the plasma (as in Fig. 8), and the $-$ sign would apply if \mathbf{e}_z were to point into the boundary. In Eqs. (A10)–(A11) recall that k_x and k_y are regarded as imposed (and hence the same in the plasma and vacuum regions) and k_z arises from the vacuum dispersion relation $n^2 = 1$ (or in the electrostatic limit $n^2 \approx 0$).

To check the validity of Eqs. (A10)–(A11) and gain a further understanding of their meaning, it is useful to consider two limiting cases. First, taking $\Delta \rightarrow 0$, or the magnetic field strictly parallel to the conducting wall ($\theta = \pi/2$ or $D_z \rightarrow 0$), we recover

$$n_x E_x + n_y E_y = 0, \quad (\text{A12})$$

$$n_x E_y - n_y E_x = 0, \quad (\text{A13})$$

which imply the conventional set of boundary conditions $E_x = 0 = E_y$. Second, taking the opposite limit of very large ϵ_{\parallel} and finite Δ results in the term $n_z D_z \propto E_{\parallel}$ dominating Eq. (A10) and hence forces the boundary conditions

$$E_{\parallel} = 0, \quad (\text{A14})$$

$$B_z = 0, \quad (\text{A15})$$

which will be referred to as the sheath dominated limit. It is straightforward to derive inequalities for which the sheath dominated limit pertains. For example, considering $\cos \theta \sim 1$, $E_{\parallel} \sim E_z \sim \Phi/L$, and $E_x \sim k_x \Phi$, the sheath dominated limit occurs whenever

$$L \ll \Delta \epsilon_{\parallel} \quad (\text{A16})$$

a condition which may be interpreted as saying that the sheath capacitive impedance ($4\pi\Delta/\omega$) is greater than the plasma impedance, $4\pi L/\omega\epsilon_{\parallel}$. In this event, since the sheaths and plasma are in series, and any induced voltage drops appear across the sheaths instead of the plasma, E_{\parallel} on the plasma side must vanish.

¹F. W. Perkins, Nucl. Fusion **29**, 583 (1989).

²J. R. Myra, D. A. D'Ippolito, and M. J. Gerver, Nucl. Fusion **30**, 845 (1990).

³R. Chodura and J. Neuhauser, in *Proceedings of the 16th European Conference on Controlled Fusion and Plasma Heating*, Venice (European Physical Society, Petit-Lancy, Switzerland, 1989), Vol. 13B, Part III, p. 1089; R. Chodura, Fusion Eng. Des. **12**, 111 (1990); R. Chodura, Phys. Fluids **25**, 1628 (1982).

⁴D. A. D'Ippolito, J. R. Myra, M. Bures, and J. Jacquinot, Plasma Phys. Controlled Fusion **33**, 607 (1991), and references therein.

⁵M. Bures, J. Jacquinot, K. Lawson, M. Stamp, H. P. Summers, D. A. D'Ippolito, and J. R. Myra, Plasma Phys. Controlled Fusion **33**, 937 (1991).

⁶R. Majeski, P. Probert, T. Tanaka, D. Diebold, R. Breun, M. Doczy, R. Fonck, N. Hershkovitz, T. Intrator, G. McKee, and J. Sorenson, in *AIP Conference Proceedings 244—Radio Frequency Power in Plasmas*, Charleston, SC (American Institute of Physics, New York, 1992), p. 322.

⁷R. Van Nieuwenhove and G. Van Oost, J. Nucl. Mater. **162–164**, 288 (1989).

⁸D. A. D'Ippolito, J. R. Myra, J. Jacquinot, and M. Bures, in *Plasma Physics and Controlled Nuclear Fusion Research 1992* (International Atomic Energy Agency, Vienna, 1993), paper IAEA-CN-56/E-3-9; and D. A. D'Ippolito, J. R. Myra, J. Jacquinot, and M. Bures, Phys. Fluids B **5**, 3603 (1993).

⁹P.-H. Rebut, R. J. Bickerton, and B. E. Keen, Nucl. Fusion **25**, 1011 (1985).

¹⁰M. Bures, K. Avinash, H. Brinkschulte, G. Devillers, J. Jacquinot, S. Knowlton, A. Pochelon, D. Start, and J. Tagle, Bull. APS **33**, 2032 (1988).

¹¹J. A. Tagle, M. Laux, S. Clement, S. K. Erents, H. Brinkschulte, M. Bures, and L. DeKock, Fusion Eng. Des. **12**, 217 (1990).

¹²M. Keilhacker and the ASDEX Team, Nucl. Fusion **25**, 1045 (1985).

¹³J. V. Hofmann, G. Fussmann, J.-M. Noterdaeme, and F. Ryter, Fusion Eng. Des. **12**, 185 (1990).

¹⁴F. W. Perkins, Bull. Am. Phys. Soc. **34**, 2093 (1989), Paper 6S6.

¹⁵E. Berro, B. Fried, D. Holland, and G. Morales (private communication, 1988).

¹⁶M. Brambilla, R. Chodura, J. Hoffmann, J. Neuhauser, J.-M. Noterdaeme, F. Ryter, R. Schubert, and F. Wesner, in *Plasma Physics and Controlled Nuclear Fusion Research 1990* (International Atomic Energy Agency, Vienna, 1991), Vol. I, p. 723; and M. Brambilla and J.-M. Noterdaeme, in *Proceedings of the 17th European Conference on Controlled Fusion and Plasma Heating*, Amsterdam (European Physical Society, Petit-Lancy, Switzerland, 1990), Vol. 14B, Pt. III, p. 1056.

¹⁷J. R. Myra and D. A. D'Ippolito, in *Proceedings of the Tenth APS Topical Conference on Applications of Radio-Frequency Power to Plasmas*, Boston, MA (American Institute of Physics, New York, 1994), p. 421.

¹⁸J. Bohdansky, in Nucl. Fusion Special Issue, **24**, 61 (1984) and errata in Nucl. Fusion **24**, 1683 (1984).